# Background-free detection of molecular chirality using a single-color beam [Invited]

Yuhang Chen (陈宇航)[1], Xiaosong Zhu (祝晓松)[1*], Pengfei Lan (兰鹏飞)[1**], and Peixiang Lu (陆培祥)[1,2]

[1] Wuhan National Laboratory for Optoelectronics and School of Physics, Huazhong University of Science and Technology, Wuhan 430074, China

[2] Optics Valley Laboratory, Wuhan 430074, China

*Corresponding author: zhuxiaosong@hust.edu.cn
**Corresponding author: pengfeilan@hust.edu.cn

We propose and numerically demonstrate a simple and background-free all-optical chiral spectroscopy technique for gas molecules. Our approach is based on high harmonic generation driven by a new type of laser beam that is produced by one linearly polarized single-color beam passing through a lens and a prism. It is shown that chiral and achiral signals are completely separated in frequency, indicating strong background-free and highly sensitive chirality detection. We believe this all-optical method can open new opportunities for ultrafast detection for chiral dynamics in the femtosecond to attosecond time scale.

**Keywords:** high harmonic generation; strong-field chiral spectroscopy; selection rule.
**DOI:** 10.3788/COL202220.100004

## 1. Introduction

Chirality is a fundamental property in nature. It manifests in various physical, chemical, and biological processes[1,2]. Chiral molecules do not have a symmetry plane and exist in pairs of left- and right-handed enantiomers. Chiral molecules show strong enantiomeric selectivity[3–5]. Therefore, it is vital to identify the molecular chirality. One of the standard optical methods for chirality detection is the circular dichroism (CD) absorption spectroscopy[6], which is manifested by the difference in absorption between left-handed and right-handed circularly polarized light. Other available techniques include circular fluorescence[7] or Raman scattering[8]. However, these techniques rely on the interactions involving both the electric and magnetic components of the light field. Because the magnetic effects are weak, it makes poor chiral responses. One way around this restriction is to employ techniques that do not rely on magnetic interaction, but solely rely on electric–dipole interactions, such as Coulomb explosion imaging[9,10], microwave three-wave mixing spectroscopy[11,12], and photoelectron CD (PECD)[13–15].

In recent years, high harmonic generation (HHG) has been shown to offer an alternative approach. HHG is based on the interaction between the intense laser pulse and the medium[16–21]. It naturally offers ultrafast sub-femtosecond temporal resolution[22–26] and an all-optical detection scheme. The initial works are based on electric–magnetic interaction and still generate weak chiral signals leading to low sensitivity[27–30].

For example, the first experiment, to the best of our knowledge, only acquired 2%–3% chiral signal[27,28]. Very recently, chiral spectroscopy methods based on dynamical symmetry (DS) breaking in HHG[31–35] have been proposed. This group of methods is based only on electric components of light and shows strong chiral signals and high enantio-sensitivity. However, nearly all of them depend on the non-collinear superposition of multi-color beams, which requires a highly stable coincidence of beams in time and space in the experiment.

In this work, we show that an intense linearly polarized single-color beam can yield strong chiral signals in the high harmonic spectrum. The linearly polarized single-color beam is focused by a lens and a prism, which will generate the field being elliptically polarized in the plane of propagation, as shown in Fig. 1(b). Compared to non-collinear schemes[31–35], this scheme suggests a simpler experimental setup. Through symmetry analysis in HHG and numerical calculations by three-dimensional time-dependent density functional theory (TDDFT), we show that chiral and achiral signals in HHG are completely separated in frequency, leading to background-free and highly sensitive chirality detection. Furthermore, analysis of far-field propagation shows that the chiral signals retain in the far field. Throughout this Letter, atomic units (a.u.) are used, lowercase $\vec{r} = (x,y,z)$ denotes the molecular microscopic coordinate, and uppercase $\vec{R} = (X,Y,Z)$ represents the macroscopic coordinate of the laser beam.
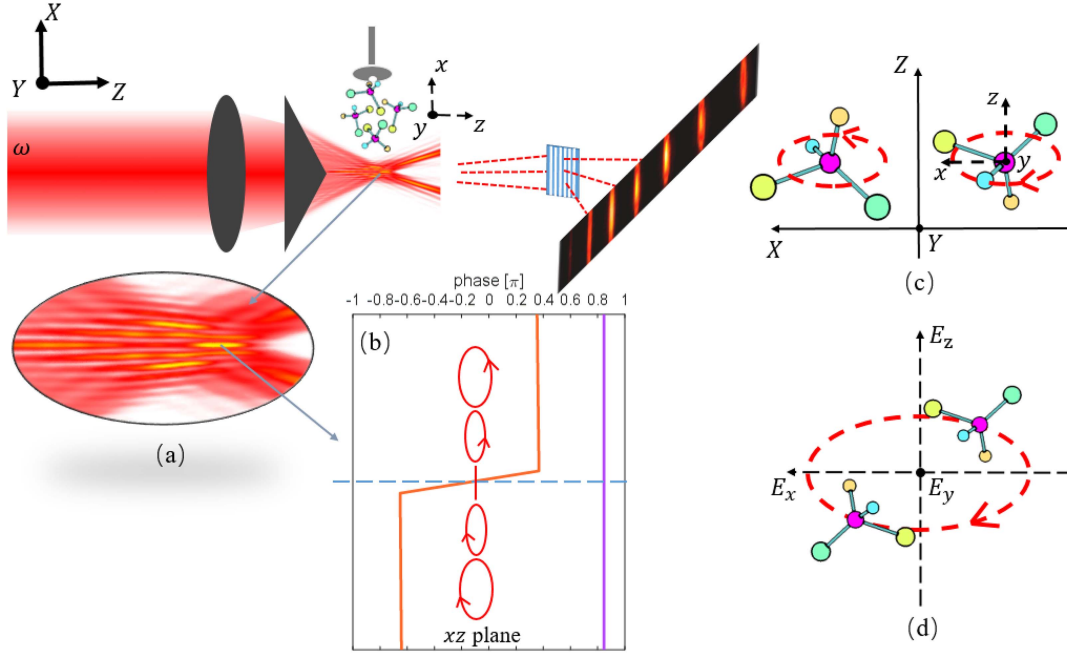
**Fig. 1.** (a) Top panel: schematic of the experimental setup. Capital $X$, $Y$, $Z$ denote the macroscopic coordinate, and lowercase $x$, $y$, $z$ denote the microscopic coordinate. Lower panel: the intensity distribution of the laser beam near the focus calculated in COMSOL, where yellow represents higher intensity. (b) The red thick circles with arrows show the Lissajou figures and rotation directions of the laser fields at different macroscopic points along the $X$ direction near the focus. Blue dashed line represents the center of the beam. Meanwhile, the phases of the $x$ and $z$ components of the laser at different macroscopic points along the $X$ direction are shown as the purple and orange lines, respectively, corresponding to the top axis. (c) Macroscopic schematic of the symmetry $\hat{R}_2^Z \cdot \hat{R}_2^x$ of the system. Any oriented molecule at an arbitrary macroscopic point $(X, 0, Z)$ can find another molecule having the same configuration as that of the former molecule rotated by $\pi$ around the $x$ axis at $(-X, 0, Z)$. The electric fields at these two points have the same ellipticity and opposite helicity, as shown by the red dotted circles. (d) Macroscopic schematic of the $\hat{C}_2^y$ symmetry of the system. Any oriented molecule can find another molecule having the same configuration as that of the former molecule rotated by $\pi$ around the $y$ axis.

## 2. Theoretical Model

HHG records the ultrafast electronic response of matter to light. As the laser wavelength is much larger than the molecular dimensions, any spatial dependence of the field is neglected in HHG. In the vicinity of a macroscopic point $\vec{R}$, where the electric field is constant, the microscopic Hamiltonian of a single molecule interacting with the laser field is given within the Born–Oppenheimer and dipole approximations by[31,36]

$$\hat{H}_{\vec{R}}^\Lambda(t) = \sum_j -\frac{\nabla_j^2}{2} + \frac{1}{2}\sum_{i \neq j} \frac{1}{|\vec{r}_i - \vec{r}_j|}$$
$$+ \sum_j V^\Lambda(\vec{r}_j) + \sum_j \vec{E}(t; \vec{R}) \cdot \vec{r}_j. \tag{1}$$

$\hat{H}_{\vec{R}}^\Lambda(t)$ is the full time-dependent multi-electron Hamiltonian. $\Lambda$ represents the molecular orientation. $\vec{r}_j$ is the microscopic coordinate of the $j$th electron. $\nabla_j^2$ is the corresponding Laplacian operator. $V^\Lambda$ is the electrostatic interactions of electrons with the nuclei.

From the time-dependent Schrödinger equation at $\vec{R}$,

$$\hat{H}_{\vec{R}}^\Lambda(t)\Psi_{\vec{R}}^\Lambda(t) = i\frac{\partial}{\partial t}\Psi_{\vec{R}}^\Lambda(t), \tag{2}$$

the time-dependent wave function $\Psi_{\vec{R}}^\Lambda(t)$ can be obtained. Then, the time-dependent dipole moment of a single oriented molecule can be written as

$$\vec{p}^\Lambda(t; \vec{R}) = \langle \Psi_{\vec{R}}^\Lambda(t)|\vec{r}|\Psi_{\vec{R}}^\Lambda(t)\rangle. \tag{3}$$

For a randomly oriented molecular ensemble in the vicinity of $\vec{R}$, the orientation average of the induced dipole moment from all orientations should be considered:

$$\vec{p}(t; \vec{R}) = \sum_\Lambda \vec{p}^\Lambda(t; \vec{R}). \tag{4}$$

This dipole moment corresponds to the effective Hamiltonian for the orientation-averaged ensemble:

$$\hat{H}_{\vec{R}}(t) = \sum_\Lambda \hat{H}_{\vec{R}}^\Lambda(t), \tag{5}$$

which exhibits a higher symmetry than $\hat{H}_{\vec{R}}^\Lambda(t)$[31].

From the second derivative and Fourier transform of the dipole moment, the harmonic spectrum is obtained:

$$\vec{S}(\Omega; \vec{R}) = \int \ddot{\vec{p}}(t; \vec{R}) e^{-i\Omega t} dt, \qquad (6)$$

where $\Omega$ is the harmonic frequency.

As it is difficult to solve the multi-electron Schrödinger equation in Eq. (1), three-dimensional TDDFT is adopted to numerically simulate the real-time response of the molecule to laser field and calculate $\vec{p}^{\Lambda}(t; \vec{R})$[35,37,38]. TDDFT is implemented with the real-space grid-based OCTOPUS code[39–41]. The calculation is performed within the local density approximation (LDA)[42]. The frozen core approximation is used for inner core orbitals, which are treated with norm-conserving pseudopotentials[43]. To simulate randomly oriented molecules, we calculate 24 orientations by setting intervals of 90 deg for each Euler angle[31]. In our calculation, the Kohn–Sham (KS) equations are solved in a spherical box with grid spacing of 0.4 a.u. and radius of 32 a.u. Time step $\Delta t = 0.05$ a.u..

## 3. Results and Discussions

We simulate the field of one Gaussian beam that propagates along the $Z$ axis and is linearly polarized along the $X$ axis passing through a lens and a prism using the beam envelope method in COMSOL Multiphysics. The wavelength of the laser is 600 nm, and the beam radius is 5 mm. The focus length of the lens is 150 mm. The vertex angle of the prism is 133 deg. In this Letter, we only consider the laser field at $Y = 0$, where the intensity maximizes. The results are shown in Fig. 1.

It is shown that the electric field near the focus is elliptically polarized in the $xz$ plane; see Fig. 1(b). The electric field located at arbitrary $\vec{R}$ is invariant under $\hat{\sigma}_{xz}$ and $\hat{C}_2^y$, where $\hat{C}_2^y = \hat{\tau}_2 \cdot \hat{R}_2^y$. $\hat{\sigma}_{xz}$ represents mirror symmetry about the $xz$ plane. $\hat{\tau}_2$ is the time-translation operator standing for translating by half-optical cycle $T/2$, where $T = 2\pi/\omega$ and $\omega$ is the optical frequency of the driving laser. $\hat{R}_2^y$ is the operator of rotation standing for rotating $\pi$ about the $y$ axis. Thus, considering a multi-cycle laser beam, the electric field of this single-color beam can be written as

$$\vec{E}(t; \vec{R}) = \begin{pmatrix} E_{0x}(\vec{R}) \cos(\omega t + \phi_x(\vec{R})) \\ 0 \\ E_{0z}(\vec{R}) \cos(\omega t + \phi_z(\vec{R})) \end{pmatrix}, \qquad (7)$$

where $\phi_{x,z}$ and $E_{0x,0z}$ are the phase and amplitude of the $x$ and $z$ components of the electric field, respectively. The amplitude and phase of the electric field vary with the macroscopic position $\vec{R}$ and can be obtained from the calculation in COMSOL.

Macroscopically, for a pair of points $(X, 0, Z)$ and $(-X, 0, Z)$, it is shown that $E_{0x}(-X, 0, Z) = E_{0x}(X, 0, Z)$, $E_{0z}(-X, 0, Z) = E_{0z}(X, 0, Z)$ and $\phi_x(-X, 0, Z) = \phi_x(X, 0, Z)$, $\phi_z(-X, 0, Z) + \pi = \phi_z(X, 0, Z)$. Thus, $\Delta\phi(-X, 0, Z) + \pi = \Delta\phi(X, 0, Z)$, where $\Delta\phi = \phi_z - \phi_x$. As a consequence, one can see that $\vec{E}(t; X, 0, Z)$ and $\vec{E}(t; -X, 0, Z)$ are equal in the ellipticity but opposite in the helicity; see Fig. 1(b). Thus, the electric field is invariant under

$\hat{R}_2^Z \cdot \hat{R}_2^x$, where $\hat{R}_2^Z$ denotes the operation on macroscopic coordinates, and $\hat{R}_2^x$ denotes the operation on microscopic coordinates. Besides, it is also invariant under other symmetries, such as $\hat{\sigma}_{YZ} \cdot \hat{R}_2^x$. However, these symmetries eventually lead to the same result. Therefore, we focus on the $\hat{R}_2^Z \cdot \hat{R}_2^x$ symmetry in the discussions below.

To analyze the selection rule of HHG associated with the symmetry of the system, we consider the Hamiltonian is periodic in $T$. It is reasonable and convenient for symmetry analysis to turn to Floquet theory[36,44–46] and the time-dependent dipole moment in Eq. (4) can be written as

$$\vec{p}(t; \vec{R}) = \sum_n \vec{F}_n(\vec{R}) \exp\left(in\frac{2\pi t}{T}\right), \qquad (8)$$

where $\vec{F}_n(\vec{R})$ are complex numbers standing for the emitted frequency components in the frequency domain.

Following the proofs in Ref. [36], once the Hamiltonian exhibits a DS $\hat{G}$, $[\hat{H}_{\vec{R}}(t), \hat{G}] = 0$, the corresponding induced dipole moment $\vec{p}(t; \vec{R})$ will also uphold the DS, $\vec{p}(t; \vec{R}) = \hat{G}\vec{p}(t; \vec{R})$. By enforcing the invariance of $\vec{p}(t; \vec{R})$ under the DS, one can derive the constrains on the $\vec{F}_n(\vec{R})$, i.e., the selection rule[36,44,45].

The DS of the Hamiltonian in Eq. (5) mainly depends on the electric field and the structural feature of the media. The significant difference between chiral and achiral randomly oriented ensembles is that any oriented molecule can find its mirror symmetric molecule in the achiral ensemble, but not in the chiral ensemble. Thus, the achiral ensemble possesses mirror symmetry, while the chiral ensemble does not. Apart from that, both of them satisfy rotational symmetry to revolve around an arbitrary axis by arbitrary degrees.

Let us firstly consider the light–matter interaction located at a macroscopic point $\vec{R}$. According to the discussion above, the Hamiltonian of the chiral ensemble is invariant under $\hat{C}_2^y$ [see Fig. 1(d)], while the Hamiltonian of the achiral ensemble is invariant under $\hat{C}_2^y$ and $\hat{\sigma}_{xz}$.

For $\hat{C}_2^y = \hat{\tau}_2 \cdot \hat{R}_2^y$ symmetry, the dipole moment satisfies $\hat{C}_2^y \vec{p}(t) = \vec{p}(t)$, namely

$$\hat{\tau}_2 \cdot \hat{R}_2^y \sum_n \vec{F}_n \exp\left(in\frac{2\pi t}{T}\right) = \sum_n \vec{F}_n \exp\left(in\frac{2\pi t}{T}\right). \qquad (9)$$

From Eq. (9), one obtains

$$\sum_n \begin{pmatrix} -F_{nx} \cdot (-1)^n \\ F_{ny} \cdot (-1)^n \\ -F_{nz} \cdot (-1)^n \end{pmatrix} = \sum_n \begin{pmatrix} F_{nx} \\ F_{ny} \\ F_{nz} \end{pmatrix}. \qquad (10)$$

Equation (10) leads to the selection rules where odd harmonics are $x$- or $z$-polarized and even harmonics are only $y$-polarized.

With similar analysis, one will conclude that, under the $\hat{\sigma}_{xz}$ symmetry, $y$-polarized harmonics are forbidden. $\hat{\sigma}_{xz}$ symmetry

is broken by the chiral ensemble, and this leads to the generation of $y$-polarized harmonics. By contrast, this symmetry is upheld in the achiral ensemble so that $y$-polarized harmonics are forbidden. Therefore, $y$-polarized even harmonics are chiral signals, i.e., they are unique for chiral targets.

As a demonstration, we numerically calculated the high harmonic response of randomly oriented chiral molecules CHFClBr driven by the strong laser field at an example macroscopic point $(-X_0, 0, 0)$ based on TDDFT. The molecular geometry of CHFClBr is from experimental measurement[47,48]. From the calculation in COMSOL, the amplitudes $E_{0x}$ and $E_{0z}$ at $(-X_0, 0, 0)$ are set as $8.08 \times 10^6\,\text{V/cm}$ and $2.18 \times 10^6\,\text{V/cm}$, corresponding to laser intensity of $7 \times 10^{13}\,\text{W/cm}^2$. The phases $\phi_x$ and $\phi_z$ are $0.85\pi$ and $-0.65\pi$. The Lissajou curve is shown in Fig. 1(d). In addition, a trapezoidal envelope with a total duration of six optical cycles (with two-cycle linear ramps and two-cycle constant center) is adopted for the laser pulse.

Figure 2 shows the HHG spectra from left-handed and racemic CHFClBr ensembles. Consistent with the symmetry analysis, $y$-polarized even harmonics are chiral signals (only
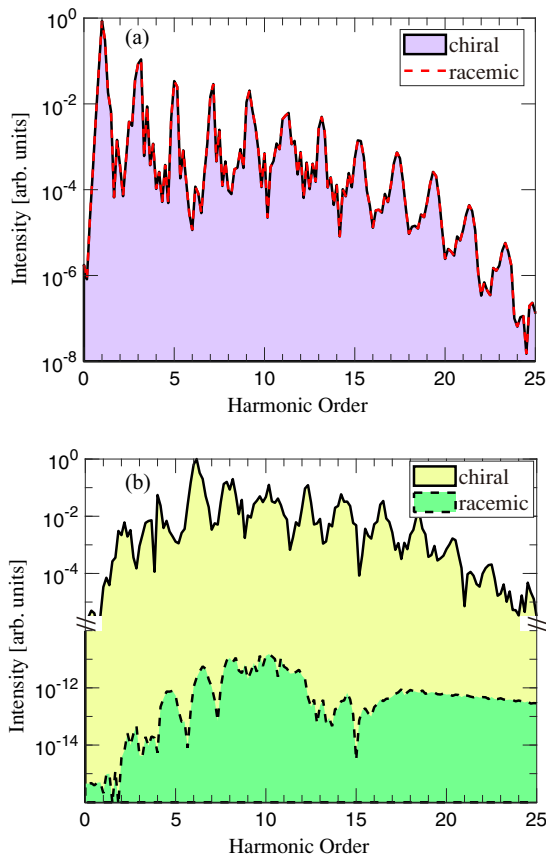


**Fig. 2.** Numerically calculated normalized intensity of (a) $x$-polarized and (b) $y$-polarized HHG emissions from the chiral and racemic ensembles based on TDDFT. For the chiral ensemble, only odd harmonics have $x$-polarized components, and only even harmonics have $y$-polarized components. But, for the racemic ensemble, there is no $y$-polarized harmonic emission, and the $x$-polarized harmonic orders are still odd. The detailed parameters are given in the Letter.

generated from the chiral ensemble), while $x$-polarized odd harmonics are achiral (obtained from either kind of ensemble). Since chiral and achiral signals are completely separated in harmonic order, the chiral signals are background-free. This leads to extremely high sensitivity to the chirality of the target media. Furthermore, the only thing one needs to focus on is observing whether there are even harmonics in the spectra. This greatly simplifies the detection setup.

Note that, since this scheme is based on the DS breaking in HHG, it is valid not only for a certain molecule or some specific parameters of the lens and prism. As long as the combination of the lens and prism induces a focused region, as shown in Fig. 1, the background-free chiral signals, i.e., even harmonics, can be generated from chiral ensembles without mirror symmetry driven by such a structured beam. Nevertheless, the intensity of the chiral signals may differ in different chiral molecules. This implies that one can detect the changes in structural chirality of a chiral molecule and the absolute value of the enantiomeric excess in mixtures of left- and right-handed molecules according to the intensity of the chiral signals.

In experiments, the signal that one detects is not the emission located in the near field, but the far-field superposition of the harmonics emitted at different macroscopic points in the interaction region between the medium and the laser. Thus, it is necessary to invesigate the relation between the HHG emissions at different macroscopic points.

As discussed above, $\vec{E}(t; \vec{R}) = \hat{R}_2^Z \cdot \hat{R}_2^x \vec{E}(t; \vec{R})$. Thus, the Hamiltonian satisfies $\hat{R}_2^Z \cdot \hat{R}_2^x$ symmetry; see Fig. 1(c). Employing the symmetry analysis method, from $\vec{p}(t; \vec{R}) = \hat{R}_2^Z \cdot \hat{R}_2^x \vec{p}(t; \vec{R})$, the following formula can be obtained:

$$\sum_n \begin{pmatrix} F_{nx}(-X, 0, Z) \\ -F_{ny}(-X, 0, Z) \\ -F_{nz}(-X, 0, Z) \end{pmatrix} = \sum_n \begin{pmatrix} F_{nx}(X, 0, Z) \\ F_{ny}(X, 0, Z) \\ F_{nz}(X, 0, Z) \end{pmatrix}. \tag{11}$$

Hence, for HHG emissions from $(-X, 0, Z)$ and $(X, 0, Z)$, the $x$-polarized harmonics (achiral signal) are in phase, while $y$-polarized harmonics (chiral signal) are out of phase. Figure 3 shows the calculated results of the phases, taking the
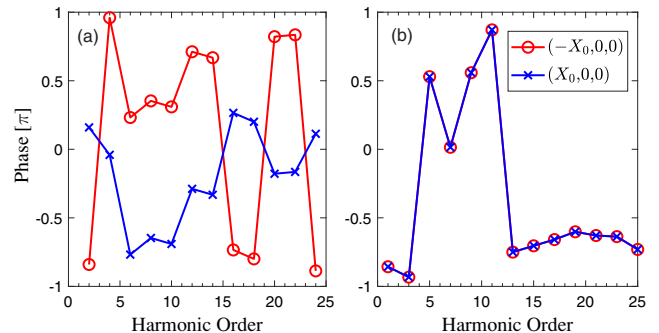


**Fig. 3.** Numerically calculated phase of (a) $y$- and (b) $x$-polarized harmonics at $(\pm X_0, 0, 0)$.
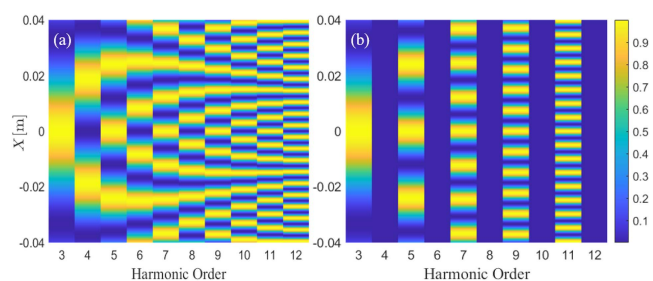
**Fig. 4.** Superposition of HHG spectra from (a) chiral ensemble and (b) racemic ensemble at $(-X_0, 0, 0)$ and $(X_0, 0, 0)$ in the far field. The maximum values are normalized to one for each harmonic.

points $(\pm X_0, 0, 0)$ as an example. The calculated results are consistent with the analysis.

Let us then consider the superposition of the harmonics emitted from these two points in the far field. The electric field at a distance $Z$ along the direction of light propagation is given by a standard Huygens–Fresnel integral[49]:

$$
\begin{aligned}
&E_{Z,\lambda_q}(X,Y) \\
&= \frac{e^{i\frac{\pi}{\lambda_q Z}(X^2+Y^2)}}{i\lambda_q Z} \int_{-\infty}^{\infty} \int_{-\infty}^{\infty} E_h(X',Y') e^{i\frac{\pi}{\lambda_q Z}(X'^2+Y'^2)} e^{\frac{-i2\pi(XX'+YY')}{Z\lambda_q}} \, dX' dY',
\end{aligned}
$$
(12)

where $(X',Y')$ and $(X,Y)$ are the coordinates at the near field and far field, respectively, $\lambda_q$ is the wavelength of the considered harmonic, and $E_h$ is the near-field harmonic electric field. We calculate the results of far-field superposition at $Z = 2$ m.

Figure 4 shows the far-field superposition of different order harmonic emissions from $(-X_0, 0, 0)$ and $(X_0, 0, 0)$. The result shows alternatively light and dark Young's double-slit interference fringes. Since the even harmonic emissions from this pair of points are out of phase, the central stripes are dark; but for the odd harmonics, they are bright because of zero phase differences. Comparing Figs. 4(a) and 4(b), one can see that even harmonics remain after the interference for the chiral ensemble, while there are still no even harmonics for the racemic ensemble. Harmonic signals emitted from any pair of points $(X, 0, Z)$ and $(-X, 0, Z)$ will also show similar figures, but the positions of the bright stripes are different. The total harmonic spectra can be understood as the superposition of the harmonics emitted from these pairs of points near the focus. Hence, in the far field, even harmonics remain detectable from chiral ensembles, while no even harmonics can be observed from achiral ensembles.

The experimental setup can be similar to normal HHG setups for a gaseous medium[27,29,30]. However, since the samples of chiral molecules are generally liquid or solid at room temperature, one has to vaporize the samples. A continuous flow of helium carrier gas should then pass through the samples to deliver the vapor to the nozzle in the chamber of the HHG setup. In order to prevent re-condensation during the delivery, the pipes of the delivery manifold and the nozzle should be kept

at a high temperature. Besides, the samples could re-condense in the chamber, and thus special attention should be paid to prevent contamination of the chamber and the detector.

## 4. Conclusion

In summary, we propose and demonstrate a linearly polarized single-color beam passing through a lens, and a prism can yield strong chiral signals in HHG. Since the chiral and achiral signals are completely separated in frequency, the chiral signals are background-free. Without requirement for space–time stabilization between the non-collinear multi-color lasers, our approach offers a simple and compact all-optical experimental setup. This technique opens new opportunities for quantitative detection of chirality and ultrafast chiral dynamics with ultrahigh sensitivity and temporal resolution.

## References and Note

1. J. Gal, "The discovery of stereoselectivity at biological receptors: Arnaldo Piutti and the taste of the asparagine enantiomers-history and analysis on the 125th anniversary," Chirality **24**, 959 (2012).
2. P. Fischer and F. Hache, "Nonlinear optical spectroscopy of chiral molecules," Chirality **17**, 421 (2005).
3. A. J. Hutt and S. C. Tan, "Drug chirality and its clinical significance," Drugs **52**, 1 (1996).
4. D. J. Abraham, J. Singh, and T. J. Hagen, "Chirality and biological activity," in *Burger's Medicinal Chemistry and Drug Discovery* (Wiley, 2010), p. 127.
5. S. Giri, A. M. Dudzinski, J. C. Tremblay, and G. Dixit, "Time-dependent electronic current densities in chiral molecules," Phys. Rev. A **102**, 063103 (2020).
6. N. Berova, P. L. Polavarapu, K. Nakanishi, and R. W. Woody, *Comprehensive Chiroptical Spectroscopy: Applications in Stereochemical Analysis of Synthetic Compounds, Natural Products, and Biomolecules* (Wiley, 2012).
7. E. Castiglioni, S. Abbate, F. Lebon, and G. Longhi, "Chiroptical spectroscopic techniques based on fluorescence," Methods Appl. Fluoresc. **2**, 024006 (2014).
8. V. Parchaňský, J. Kapitán, and P. Bouř, "Inspecting chiral molecules by Raman optical activity spectroscopy," RSC Adv. **4**, 57125 (2014).
9. M. Pitzer, M. Kunitski, A. S. Johnson, T. Jahnke, H. Sann, F. Sturm, L. PH. H. Schmidt, H. Schmidt-Böcking, R. Dörner, J. Stohner, J. Kiedrowski, M. Reggelin, S. Marquardt, A. Schießer, R. Berger, and M. S. Schöffler, "Direct determination of absolute molecular stereochemistry in gas phase by Coulomb explosion imaging," Science **341**, 1096 (2013).
10. P. Herwig, K. Zawatzky, M. Grieser, O. Heber, B. Jordon-Thaden, C. Krantz, O. Novotný, R. Repnow, V. Schurig, D. Schwalm, Z. Vager, A. Wolf, O. Trapp, and H. Kreckel, "Imaging the absolute configuration of a chiral epoxide in the gas phase," Science **342**, 1084 (2013).
11. D. Patterson, M. Schnell, and J. Doyle, "Enantiomer-specific detection of chiral molecules via microwave spectroscopy," Nature **497**, 475 (2013).

12. S. Eibenberger, J. Doyle, and D. Patterson, "Enantiomer-specific state transfer of chiral molecules," Phys. Rev. Lett. **118**, 123002 (2017).

13. N. Böwering, T. Lischke, B. Schmidtke, N. Müller, T. Khalil, and U. Heinzmann, "Asymmetry in photoelectron emission from chiral molecules induced by circularly polarized light," Phys. Rev. Lett. **86**, 1187 (2001).

14. A. Comby, S. Beaulieu, M. Boggio-Pasqua, D. Descamps, F. Légaré, L. Nahon, S. Petit, B. Pons, B. Fabre, Y. Mairesse, and V. Blanchet, "Relaxation dynamics in photoexcited chiral molecules studied by time-resolved photoelectron circular dichroism: toward chiral femtochemistry," J. Phys. Chem. Lett. **7**, 4514 (2016).

15. S. Beaulieu, A. Comby, A. Clergerie, J. Caillat, D. Descamps, N. Dudovich, B. Fabre, R. Géneaux, F. Légaré, S. Petit, B. Pons, G. Porat, T. Ruchon, R. Taïeb, V. Blanchet, and Y. Mairesse, "Attosecond-resolved photoionization of chiral molecules," Science **358**, 1288 (2017).

16. P. B. Corkum, "Plasma perspective on strong field multiphoton ionization," Phys. Rev. Lett. **71**, 1994 (1993).

17. A. D. Shiner, B. E. Schmidt, C. Trallero-Herrero, H. J. Wörner, S. Patchkovskii, P. B. Corkum, J.-C. Kieffer, F. Légaré, and D. M. Villeneuve, "Probing collective multi-electron dynamics in xenon with high-harmonic spectroscopy," Nat. Phys. **7**, 464 (2011).

18. S. Ghimire, A. DiChiara, E. Sistrunk, P. Agostini, L. F. DiMauro, and D. A. Reis, "Observation of high-order harmonic generation in a bulk crystal," Nat. Phys. **7**, 138 (2011).

19. W. Xiong, J. Geng, J. Tang, L. Peng, and Q. Gong, "Mechanisms of below-threshold harmonic generation in atoms," Phys. Rev. Lett. **112**, 233001 (2014).

20. L. Li, P. Lan, X. Zhu, T. Huang, Q. Zhang, M. Lein, and P. Lu, "Reciprocal-space-trajectory perspective on high-harmonic generation in solids," Phys. Rev. Lett. **122**, 193901 (2019).

21. L. Li, P. Lan, X. Zhu, and P. Lu, "Huygens-Fresnel picture for high harmonic generation in solids," Phys. Rev. Lett. **127**, 223201 (2021).

22. S. Baker, J. S. Robinson, C. A. Haworth, H. Teng, R. A. Smith, C. C. Chirila, M. Lein, J. W. G. Tisch, and J. P. Marangos, "Probing proton dynamics in molecules on an attosecond time scale," Science **312**, 424 (2006).

23. O. Smirnova, Y. Mairesse, S. Patchkovskii, N. Dudovich, D. Villeneuve, P. Corkum, and MY. Ivanov, "High harmonic interferometry of multi-electron dynamics in molecules," Nature **460**, 972 (2009).

24. L. He, P. Lan, A. Le, B. Wang, B. Wang, X. Zhu, P. Lu, and C. D. Lin, "Real-time observation of molecular spinning with angular high-harmonic spectroscopy," Phys. Rev. Lett. **121**, 163201 (2018).

25. L. He, Q. Zhang, P. Lan, W. Cao, X. Zhu, C. Zhai, F. Wang, W. Shi, M. Li, X. Bian, P. Lu, and A. D. Bandrauk, "Monitoring ultrafast vibrational dynamics of isotopic molecules with frequency modulation of high-order harmonics," Nat. Commun. **9**, 1108 (2018).

26. L. Li, T. Huang, P. Lan, J. Li, Y. Zhang, X. Zhu, L. He, W. Cao, and P. Lu, "Fingerprint of the interbond electron hopping in second-order harmonic generation," Phys. Rev. Lett. **128**, 027401 (2022).

27. R. Cireasa, A. E. Boguslavskiy, B. Pons, M. C. H. Wong, D. Descamps, S. Petit, H. Ruf, N. Thiré, A. Ferré, J. Suarez, J. Higuet, B. E. Schmidt, A. F. Alharbi, F. Légaré, V. Blanchet, B. Fabre, S. Patchkovskii, O. Smirnova, Y. Mairesse, and V. R. Bhardwaj, "Probing molecular chirality on a sub-femtosecond timescale," Nat. Phys. **11**, 654 (2015).

28. O. Smirnova, Y. Mairesse, and S. Patchkovskii, "Opportunities for chiral discrimination using high harmonic generation in tailored laser fields," J. Phys. B **48**, 234005 (2015).

29. Y. Harada, E. Haraguchi, K. Kaneshima, and T. Sekikawa, "Circular dichroism in high-order harmonic generation from chiral molecules," Phys. Rev. A **98**, 021401 (2018).

30. D. Baykusheva and H. J. Wörner, "Chiral discrimination through bielliptical high-harmonic spectroscopy," Phys. Rev. X **8**, 031060 (2018).

31. O. Neufeld, D. Ayuso, P. Decleva, M. Y. Ivanov, O. Smirnova, and O. Cohen, "Ultrasensitive chiral spectroscopy by dynamical symmetry breaking in high harmonic generation," Phys. Rev. X **9**, 031002 (2019).

32. D. Ayuso, O. Neufeld, A. F. Ordonez, P. Decleva, G. Lerner, O. Cohen, M. Ivanov, and O. Smirnova, "Synthetic chiral light for efficient control of chiral light–matter interaction," Nat. Photonics **13**, 866 (2019).

33. D. Ayuso, A. F. Ordonez, P. Decleva, M. Ivanov, and O. Smirnova, "Enantio-sensitive unidirectional light bending," Nat. Commun. **12**, 3951 (2021).

34. D. Ayuso, A. F. Ordonez, P. Decleva, M. Ivanov, and O. Smirnova, "Strong chiral response in non-collinear high harmonic generation driven by purely electric-dipole interactions," Opt. Express **30**, 4659 (2022).

35. O. Neufeld, O. Wengrowicz, O. Peleg, A. Rubio, and O. Cohen, "Detecting multiple chiral centers in chiral molecules with high harmonic generation," Opt. Express **30**, 3729 (2022).

36. O. Neufeld, D. Podolsky, and O. Cohen, "Floquet group theory and its application to selection rules in harmonic generation," Nat. Commun. **10**, 405 (2019).

37. X. Zhu, X. Liu, P. Lan, D. Wang, Q. Zhang, W. Li, and P. Lu, "Anomalous circular dichroism in high harmonic generation of stereoisomers with two chiral centers," Opt. Express **24**, 24824 (2016).

38. D. Wang, X. Zhu, X. Liu, L. Li, X. Zhang, P. Lan, and P. Lu, "High harmonic generation from axial chiral molecules," Opt. Express **25**, 23502 (2017).

39. M. A. L. Marques, A. Castro, G. F. Bertsch, and A. Rubio, "Octopus: a first-principles tool for excited electron-ion dynamics," Comput. Phys. Commun. **151**, 60 (2003).

40. A. Castro, H. Appel, M. Oliveira, C. A. Rozzi, X. Andrade, F. Lorenzen, M. A. L. Marques, E. K. U. Gross, and A. Rubio, "Octopus: a tool for the application of time-dependent density functional theory," Phys. Stat. Sol. **243**, 2465 (2006).

41. X. Andrade, D. Strubbe, U. De Giovannini, A. H. Larsen, M. J. T. Oliveira, J. Alberdi-Rodriguez, A. Varas, I. Theophilou, N. Helbig, M. J. Verstraete, L. Stella, F. Nogueira, A. Aspuru-Guzik, A. Castro, M. A. L. Marques, and A. Rubio, "Real-space grids and the Octopus code as tools for the development of new simulation approaches for electronic systems," Phys. Chem. Chem. Phys. **17**, 31371 (2015).

42. J. P. Perdew and A. Zunger, "Self-interaction correction to density-functional approximations for many-electron systems," Phys. Rev. B **23**, 5048 (1981).

43. C. Hartwigsen, S. Goedecker, and J. Hutter, "Relativistic separable dual-space Gaussian pseudopotentials from H to Rn," Phys. Rev. B **58**, 3641 (1998).

44. O. E. Alon, V. Averbukh, and N. Moiseyev, "Selection rules for the high harmonic generation spectra," Phys. Rev. Lett. **80**, 3743 (1998).

45. X. Liu, X. Zhu, L. Li, Y. Li, Q. Zhang, P. Lan, and P. Lu, "Selection rules of high-order-harmonic generation: symmetries of molecules and laser fields," Phys. Rev. A **94**, 033410 (2016).

46. X. Zhu, P. Lu, and M. Lein, "Control of the geometric phase and nonequivalence between geometric-phase definitions in the adiabatic limit," Phys. Rev. Lett. **128**, 030401 (2022).

47. R. D. Johnson, III, "NIST computational chemistry comparison and benchmark database," https://cccbdb.nist.gov/.

48. Left-handed CHFClBr:C(0,0,0); H(0.0592,1.0771,0.1417); Cl(1.2383, −0.4784,−1.1326); F(0.2048,−0.6098,1.1937); Br(−1.7683,−0.4376, −0.6315). Here, angstroms are used.

49. R. Géneaux, A. Camper, T. Auguste, O. Gobert, J. Caillat, R. Taïeb, and T. Ruchon, "Synthesis and characterization of attosecond light vortices in the extreme ultraviolet," Nat. Commun. **7**, 12583 (2016).